Injection characteristics and fuel-air mixing process of ammonia jets in a constant volume vessel

Zhang, Zhifei; Li, Tie; Chen, Run; Wang, Ning; Wei, Yijie; Wu, Dawei

DOI:
10.1016/j.fuel.2021.121408

Document Version
Peer reviewed version

Citation for published version (Harvard):
Zhang, Z, Li, T, Chen, R, Wang, N, Wei, Y & Wu, D 2021, 'Injection characteristics and fuel-air mixing process of ammonia jets in a constant volume vessel', *Fuel*, vol. 304, 121408. https://doi.org/10.1016/j.fuel.2021.121408

Cover page

Title:

Injection characteristics and fuel-air mixing process of ammonia jets in a constant volume vessel

Authors and affiliations:

Zhifei Zhang[1], Tie Li[1, 2*], Run Chen[1, 2], Ning Wang[1], Yijie Wei[1], Dawei Wu[3]

1 State Key Laboratory of Ocean Engineering, Shanghai Jiao Tong University

2 Collaborative Innovation Center for Advanced Ship and Deep-Sea Exploration

Shanghai Jiao Tong University

3 Department of Mechanical Engineering, University of Birmingham

*Corresponding address:

Tie Li

Mulan Building B521, Shanghai Jiao Tong University

800 Dong Chuan Rd., Shanghai200240, P.R. China

Tel: +86-21-3420-8348, Fax: +86-21-3420-8348

Email: litie@sjtu.edu.cn

Injection characteristics and fuel-air mixing process of ammonia jets in a constant volume vessel

Zhifei Zhang[1], Tie Li[1, 2*], Run Chen[1, 2], Ning Wang[1], Yijie Wei[1], Dawei Wu[3]

1. State Key Laboratory of Ocean Engineering, Shanghai Jiao Tong University
2. Collaborative Innovation Center for Advanced Ship and Deep-Sea Exploration, Shanghai Jiao Tong University
3. Department of Mechanical Engineering, University of Birmingham

Abstract

The direct-injection of gaseous ammonia is a possible way to fuel engines to meet the scenario of zero-carbon emission. In this study, for the first time, the injection characteristics and fuel-air mixing process of ammonia jets are investigated. A Schlieren system is employed to characterize the macroscopic behavior of ammonia jets including the tip penetration and jet angle. Besides, the fuel concentrations of ammonia jets are quantitatively measured by LIBS to investigate the fuel-air mixing processes. According to the time evolutions of jet tip penetration, the three-stage behavior, namely the t, $t^{0.5}$ and $(t-\tau)^{0.25}$ dependence corresponding to the early stage of injection, quasi-steady stage and after two times of injection duration respectively, are proposed and the mechanisms are discussed in detail. The effects of both injection and ambient pressures on the tip penetration and jet angle, as well as the fuel concentration distributions are investigated. The increased injection pressure leads to increases in the tip penetration and fuel concentration but decreases in the jet angle. The effects of ambient pressure are opposite, indicating that the ammonia jet development is governed by the injection-to-ambient pressure ratio. The comparisons between ammonia and methane jets are conducted. The results show they have quite similar tip penetrations and jet angles, as well as the nearly equivalent fuel mole fractions at the jet axis. However, the equivalence ratios in ammonia jets are significantly lower than those in methane jets, leading to the distinct flammable mixture distributions in ammonia and methane jets.

Keywords: Carbon-free fuel; Ammonia jet; Schlieren imaging; Tip penetration; Mixing processes.

1. Introduction

The main goal of the Paris Agreement unanimously adopted in the Conference of Parties 21 (COP21) in December 2015 is to hold the increase in the global average temperature to well below 2 °C above pre-industrial levels [1]. To fulfill the Paris Agreement, it requires decarbonization of energy production by using carbon-neutral and carbon-free fuels produced from renewable energy. The production of most renewable energy sources such as wind, tidal and solar energy is intermittent [2]. Hydrogen is a carbon-free fuel with favorable combustion characteristics and thus is considered to be one of the most promising clean fuels [3]. However, the long-distance transportation and large-scale storage of hydrogen remain unsolved issues, making it difficult for widespread use, especially for powering mobility purposes.

Ammonia is considered as one of attractive carbon-free fuels due to its hydrogen-rich characteristic (up to 17.8% hydrogen by mass basis) [4]. Moreover, in comparison to hydrogen, ammonia is possible for liquefication at room temperature conditions and lower production cost, significantly in favor of storage and transportation, as well as large-scale production [5]. Nowadays, ammonia has been widely used as fertilizer in the agricultural sector, refrigerant industrial coolers, and chemical additives for the selective catalytic reduction (SCR) of the NO_x emissions in internal combustion engines (ICEs). The utilization of ammonia as a fuel in vehicle engines can date back to World War II [6]. Due to the lack of diesel fuel in Belgium in 1942, engines fueled by ammonia have been developed to maintain the bus system. After World War II, the oil supply was restored, and therefore the researches on ammonia-fueled engines were greatly reduced. In recent years, in order to moderate the global warming, ammonia-fueled engines have attracted more and more attention around the world as a promising technology [4, 7, 8].

Many literatures have so far reported ammonia's practical application in both the spark-ignition (SI) and compression-ignition (CI) engines. Compared to gasoline, ammonia has higher octane rating (~130) and thus

better anti-knock performance. This provides the potentials to improve the thermal efficiency and output power of SI engines by achieving a higher compression ratio [9]. More importantly, ammonia-fueled engines can achieve nearly zero-carbon emission in principle, which complies with the current requirements for decarbonization. However, the drawbacks of ammonia combustion are characterized by the low laminar burning velocity, low flame temperature, narrow flammability range, and high resistance to auto-ignition [10-12], making it difficult to use pure ammonia as a fuel in ICEs. As a consequence, a secondary fuel with good combustion properties is required to improve the lower combustion intensity of ammonia. Generally, the combustion promoters employed in the previous studies can be divided into two categories: hydrogen [13-16] and carbon-based fuels, such as diesel fuel [17-22], gasoline [23-25], dimethyl ether (DME) [26, 27], etc. Since both ammonia and hydrogen are gaseous under atmospheric pressure, they can be directly mixed and then introduced into the cylinder by port-fuel injection (PFI), and minor engine modifications are required to achieve the favorable combustion of ammonia. Many researchers have attempted to employ hydrogen as the combustion promoter in both ammonia-fueled SI and CI engines. Mørch et al. [9] found that the utilization of ammonia-hydrogen mixture leads to the higher efficiency and output power compared to gasoline due to the higher compression ratio. In their study, a fuel mixture with 10% hydrogen by volume fraction provided the highest efficiency and power. Pochet et al. [14] explored the combustion of an ammonia-hydrogen mixture under the homogeneous charge compression ignition (HCCI) mode in a 16:1 compression ratio engine. In their study, stable combustion was achieved with up to 70% ammonia by volume fraction. The introduction of exhaust gas recirculation (EGR) can reduce the NOx emissions but degrades the combustion efficiency due to the lower in-cylinder temperature.

Because of the poor solubility of liquid ammonia in gasoline and diesel, it is difficult to directly blend ammonia with gasoline or diesel. Therefore, when gasoline or diesel is used as the combustion promoter, the

dual-fuel strategy is usually adopted to implement ammonia combustion. Reiter and Kong [17] investigated the combustion and emission characteristics of a CI engine using a dual-fuel approach with PFI of ammonia and direct-injection (DI) of diesel. They found that the CO_2 and soot emissions were significantly decreased with the increased ammonia under the same torque output. When ammonia accounted for less than 40% of the total fuel energy, the NO_X emission was also reduced because the lower flame temperature led to the decreased thermal NO_X. Moreover, it is noted that the DI of gaseous ammonia in a SI engine has been attempted by Ryu et al. [24]. The PFI of gasoline was employed to initiate combustion and then gaseous ammonia was directly injected into the cylinder. They found that the overall brake-specific energy consumption using gasoline-ammonia is comparable to that using pure gasoline. Besides, the CO emission was observed to decrease, however, the NO_X and HC emissions were increased. Gross and Kong [26] developed a high-pressure mixing tank to blend liquid ammonia with DME and investigated the combustion and emission characteristics in a CI engine. Their results showed that the addition of ammonia to DME leads to the lower combustion pressure and temperature, and therefore the higher CO and HC emissions. The NO_X emission is also increased due to the formation of fuel NO_X, which however can be improved by increasing the injection pressure.

From the above literature review, although the utilization of pure ammonia as a fuel in engines is very challenging, it is of great significance for the requirements of zero-carbon emission and control of global temperature rise. Compared with PFI method, the gaseous ammonia DI strategy seems to be the more promising way to achieve pure ammonia combustion in engines, however, the relevant studies are quite few. The premixed combustion in PFI might cause significant unburned ammonia due to its quite low laminar flame speed. The DI diffusion combustion could reduce the unburned ammonia and therefore decrease ammonia slip which can cause air pollution and hazard to health. In addition, the PFI of gaseous ammonia will displace a certain amount of air delivered to the combustion chamber, reducing the volumetric efficiency and therefore

112 the output power of engines, while the DI of gaseous ammonia has more potentials for maintaining the charging
113 efficiency and engine power.

114 As a consequence, we aim at developing the pure-ammonia-fueled engines by the DI of gaseous ammonia
115 into the cylinder, which has the potentials to decrease ammonia slip and increase the output power. To realize
116 the DI of gaseous ammonia in engines, it is essential to make clear of the injection characteristics and the
117 ammonia-air mixing process of ammonia jets. To the best of the present authors' knowledge, this is the first
118 study on investigating the injection and mixing characteristics of gaseous ammonia jets. For this purpose, the
119 ammonia jets were captured by a high-speed Schlieren imaging system to analyze the macroscopic
120 characteristics including tip penetration and jet angle. Moreover, the fuel concentrations in ammonia jets were
121 quantitatively measured by the laser-induced breakdown spectroscopy (LIBS) technique to study the ammonia-
122 air mixing process.

123 The paper is structured as follows. The experimental systems including the Schlieren imaging and the
124 LIBS measurement technique are firstly described. Then, the image processing and definitions of jet
125 characteristics including tip penetration and jet angle are illustrated. After the time-resolved tip penetration is
126 analyzed, the effects of injection pressure and ambient pressure on both tip penetration and jet angle are
127 investigated. The pre-calibrations between the peak intensity ratio (PIR) and equivalence ratio (ϕ) are built up,
128 followed by the detailed analysis on the shot-to-shot fluctuations of equivalence ratio in ammonia jets. Then,
129 the effects of injection pressure and ambient pressure on fuel concentrations in ammonia jets are confirmed.
130 During the above analysis, meanwhile, the characteristics of DI ammonia jets are also used to compare with
131 those of methane jets. Finally, the major conclusions are summarized.

132 **2. Experimental apparatus and procedure**

133 *2.1. Constant volume vessel and fuel injection*

134 Figure 1 shows the schematic of the Schlieren imaging setup for gas jets. An optically-accessible constant
135 volume vessel (CVV) was designed to visualize the gas injections under various ambient and injection
136 conditions. The CVV provided three optical windows with 90-mm diameters [28]. A single-hole swirl injector
137 with a hole diameter of 0.93 mm was installed on the top of the CVV. A gas cylinder was connected to the
138 injector to supply the fuel gas. During the test, the air was firstly introduced into the CVV with the ambient
139 pressure (P_a) monitored by a piezo-resistive pressure sensor. Then, the fuel gas from the high-pressure gas
140 cylinder was relieved to the targeted injection pressure (P_{inj}) by a pressure regulator and then injected into the
141 CVV in the gaseous state. After each injection, the CVV was fully purged by the fresh air. The measurements
142 were performed at the room temperature of 298 K, and the saturated vapor pressure of ammonia is 10.0 bar.
143 To avoid the liquefaction of ammonia gas, the injection pressures were varied from 4.0 to 8.0 bar. Although
144 the employed injection pressures are relatively low, a previous study showed that the jet characteristics were
145 mainly dependent on the pressure ratio (PR) rather than the absolute injection pressure [29]. The PR is defined
146 as the ratio between the injection pressure and the ambient pressure, and it ranges from 2.0 to 8.0 in this study.
147 When the PR is larger than the critical value (1.9 for ammonia calculated by $(\frac{\gamma+1}{2})^{\frac{\gamma}{\gamma-1}}$, considering the
148 specific heat ratio as 1.313 for ammonia), the jet is chocked and become underexpanded. The employed
149 ambient pressures are lower than the cylinder pressure near the top dead center in DI gas engines. However,
150 due to the low volumetric energy density of gaseous ammonia, a relatively long injection duration may be
151 required to ensure that sufficient fuel is injected into the cylinder. The most importance is that, in some
152 injection strategies in gas engines, the injection timing is quite advanced (approximately either near the TDC
153 of intake process or the initial compression process) to ensure the enough mixing time because the mixing

process in gas jets is less efficient than that in liquid sprays. As a consequence, the cylinder pressure during the injection period goes through a wide range of ambient pressures. The Reynolds number at the nozzle exit is estimated by assuming the isentropic flow in the nozzle [30]. At the injection pressure of 8.0 bar and the supply fuel temperature of 298 K, the Reynolds number at the nozzle exit for ammonia jets is about 130000. The injection duration (τ) was set to 2.0 ms during all measurements. In addition to the ammonia, the injections of methane were also conducted for comparisons. The experimental conditions are summarized in Table 1.

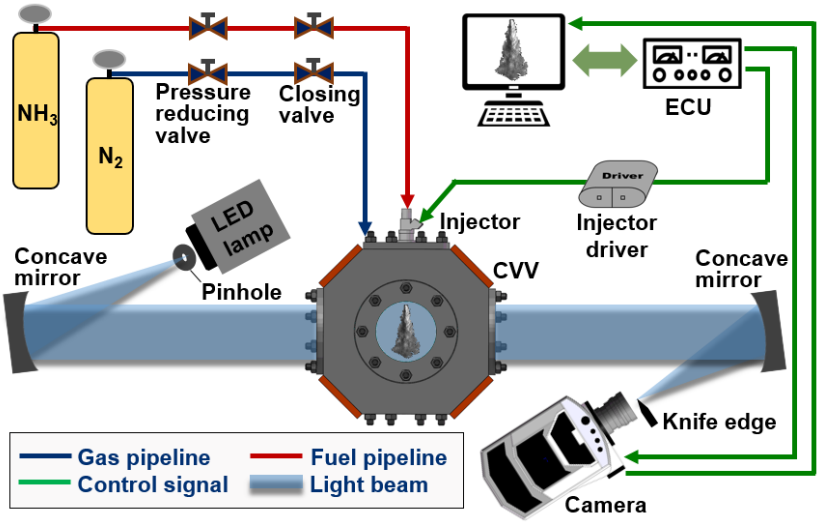

Fig. 1. Schematic of the Schlieren imaging setup for gas jets.

Table 1 Experimental conditions

Fuel type	NH_3 (base), CH_4 (comparison)
Ambient temperature (K)	298
Ambient pressure (bar)	1.0-4.0
Injector hole diameter (mm)	0.93
Injection pressure (bar)	4.0-8.0
Injection duration (ms)	2.0
Room temperature (K)	298

2.2. Schlieren imaging system

The time evolutions of ammonia jets inside the CVV were recorded using a Z-type high-speed Schlieren imaging technique. The Schlieren technique enables to detect the boundary between the gas jet and the ambient

gas due to the difference in refractive index, and therefore to investigate the macroscopic characteristics of gas jets. As shown in Fig. 1, the light from a light-emitting diode (LED) lamp was transformed into a point light source by a pinhole. Then, the light beam was collimated by a concave mirror with 500-mm focal length. The parallel light passed through gas jets in the CVV and transmitted the information of jet characteristics to the high-speed camera (Phantom V2012) through a concave mirror with 500-mm focal length and a knife-edge at the focus. Jet images were recorded at a speed of 50000 frames per second and a resolution of 512×256 pixels. The frame exposure was set to 5 μs. By using a 50-mm Nikon f/1.4 lens, the projected pixel size of the camera is 0.15 mm/pixel. The synchronization of injection and imaging was achieved by a programmable electronic control unit (ECU).

2.3. Image processing and definitions of jet characteristics

For the image processing of Schlieren images, the background images were firstly taken before the gas injections. After the fuel gas was injected, there were significant density gradients in the jets, causing variations of pixel intensity in the jet region. Then, the absolute values of the differences between the background images and the jet images were calculated. After a 3×3 pixel median filtering was implemented to improve the signal-to-noise ratio (SNR), the Canny edge detection algorithm was employed to detect the jet boundary [31]. This algorithm is based on finding the local maximum of intensity gradient in the jet image, and it enables to distinguish unclear edges. The binary images obtained from the Canny algorithm were further processed by dilation and filling operations to identify the jet region. After the jet region was determined, the jet characteristics including tip penetration, jet angle, and jet volume were analyzed. Figure 2 depicts the definitions of tip penetration and jet angle of ammonia jets. The tip penetration (S) is defined as the distance from the nozzle hole exit to the jet front edge. It should be noted that the jet has a certain width at the nozzle

exit, which cannot be ignored when determining the jet angle, especially for the first few jet images. Therefore, the jet angle (α) is evaluated by considering the upper half of the jet's projection area as an isosceles trapezoid instead of a triangle. Then the jet angle can be calculated by:

$$\alpha = \frac{360}{\pi}\arctan\frac{4A-2dS}{S^2} \quad (1)$$

where d is the nozzle hole diameter [mm] and A is the upper half of the jet's projection area [mm^2] determined based on the binary image.

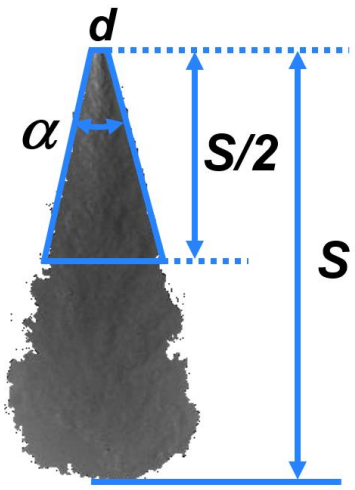

Fig. 2. Definitions of tip penetration and jet angle.

2.4. LIBS concentration measurement system

Fuel concentration information is crucial since it characterizes the fuel-air mixing and determines not only the ignition process but also the combustion process. In this study, the LIBS technique was employed to quantitatively measure the fuel concentrations in ammonia jets. The LIBS technique is an atomic emission spectroscopic technique. A high-energy laser pulse is tightly focused on the target and the resulting plasma emission is dispersed and analyzed. Compared with other laser-based techniques, the LIBS technique has

particular advantages, including the excellent SNR, high precision in quantification, independence on the molecules, and diversity of fuel forms such as solids, liquids, and gases.

The schematic of the LIBS measurement system is shown in Fig. 3. The laser beam with 6.5-mm diameter from a 532-nm Nd:YAG laser (Quantel Q-smart 450) was firstly expanded to 50 mm in diameter and then focused into the CVV using a 200-mm focal length plano-convex lens. The pulse energy (E) before the focusing lens was about 137 mJ with a standard deviation of 2.9%. The plasma emission was collected by a 100-mm focal length lenticular lens and then coupled into an optical bundle. The plasma signal was dispersed by a spectrometer (Princeton Instruments SP2500) with a 150-grooves/mm diffraction grating and finally imaged on an intensified charge-coupled device (ICCD) camera (Princeton Instruments PI MAX4). The delay and width of the ICCD gate were optimized to be 0.4 and 0.5 μs respectively, according to the signal-to-background ratios (SBRs) of atomic lines and the stability of the PIR. The detailed information can be found in our previous study [32].

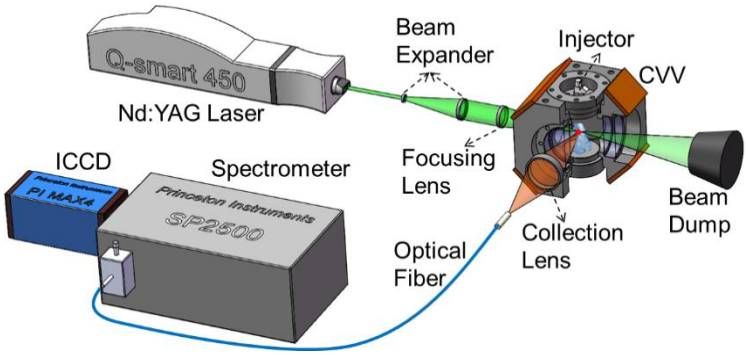

Fig. 3. Schematic of the LIBS measurement system.

In the LIBS calibrations, the ammonia and the nitrogen as a substitute of the air from high-pressure gas bottles were sequentially transferred to the CVV to produce the homogeneous mixture of a certain equivalence ratio. The equivalence ratios of the mixture were estimated by assuming a 21% O_2 ambient and the partial pressure law. A motor-driven mixing fan was employed to enable the mixture as homogeneous as possible.

Then, the laser-induced breakdowns (LIB) were generated in the homogeneous mixture and the corresponding emission spectra were analyzed. For the LIBS measurements in ammonia jets, the CVV was firstly purged. After that, the nitrogen as the ambient gas was introduced into the CVV to the targeted pressure and then the gaseous ammonia was injected. At a certain time after the start of injection, the laser shot was emitted. After the emission spectrum was collected, the equivalence ratio can be determined by the peak intensity ratio (PIR).

Figure 4 shows the LIBS spectra of the ammonia-nitrogen mixture at the ambient pressures of 1.0 bar and 4.0 bar. The equivalence ratio of the mixture is 0.95. The spectra are the average of 100 laser shots. It can be observed that the atomic lines of hydrogen and nitrogen dominate the emission spectra during the collection time of the ICCD. The hydrogen line at 656 nm, named H656 can be regarded as an indicator of ammonia gas. In addition, the strongest nitrogen line in N(I) band at 746.8 nm, termed N746 was employed to quantify the nitrogen atoms, which originate from both ammonia and ambient nitrogen. The peak intensity ratio (PIR) of H656 and N746 was employed to determine the equivalence ratio of the mixture. At the ambient pressure of 4.0 bar, the baseline continuum emission is slightly increased as a result of the denser molecules and the intensified collisions. However, the line intensity of H656 remarkably reduces due to the stronger self-absorption effects at the higher gas pressure.

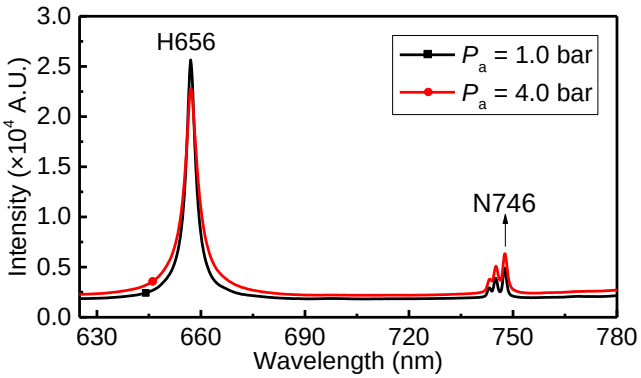

Fig. 4. The LIBS spectra of ammonia-nitrogen mixture at the ambient pressures of 1.0 bar and 4.0 bar (T_a = 298 K, ϕ = 0.95, E = 137 mJ).

2.5. Pre-calibrations of the LIBS measurement

To quantify fuel concentrations in the ammonia jets by LIBS, the pre-calibration is a necessity. The calibrations were performed by firstly producing a homogeneous ammonia-nitrogen mixture, achieving emission spectra from the laser-induced plasma in the mixture, and then constructing correlations between the intensity ratios of atomic lines and the concentration ratios of targeted atoms.

Figure 5 shows the LIBS calibration curves between the PIRs of H656/N746 and the equivalence ratios of ammonia-nitrogen mixture at different ambient pressures. Ten equivalence ratios ranging from 0.3 to 4.7 were investigated, and a hundred tests were conducted at each equivalence ratio. The PIRs of H656/N746 are the averaged results and the error bars of PIRs represent the standard deviations for the average of a hundred shots. Generally, the PIRs increase with the equivalence ratio increasing at all ambient pressures. The correlations between PIRs and equivalence ratios show nonlinear behaviors because nitrogen atoms are from both the ambient nitrogen molecule and ammonia. It is also observed that the PIRs decrease with the increased ambient pressure. This is mainly attributed to the difference in the self-absorption effects on H656 and N746. The self-absorption effects for H656 line are more prominent than N746 line due to the higher transition probability. As the ambient gas pressure increases, the self-absorption is intensified, and therefore the line intensity of H656 reduces more significantly than that of N746 [33].

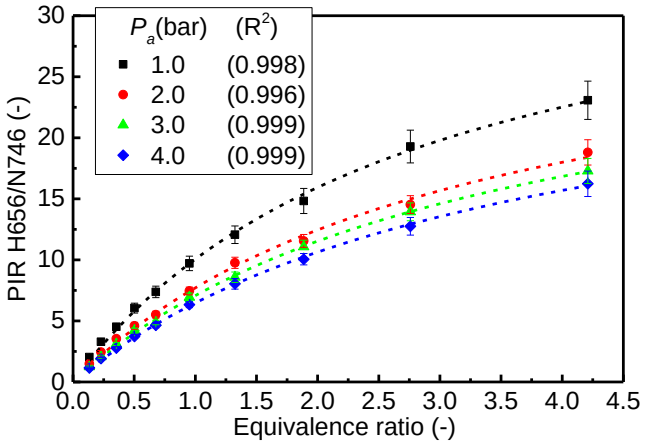

Fig. 5. The calibration curves between the PIRs of H656/N746 and the equivalence ratios of ammonia-nitrogen mixture at different ambient pressures (T_a = 298 K, E = 137 mJ).

The equivalence ratio of ammonia-nitrogen mixture is calculated by the following reaction:

$$NH_3 + 0.75O_2 = 1.5H_2O + 0.5N_2 \quad (2)$$

When considering the pure nitrogen as the ambient air with 21% oxygen, the mole ratio of ammonia and nitrogen can be expressed as:

$$n_{NH_3}/n_{N_2} = \frac{0.21}{0.75}\phi \quad (3)$$

where n_{NH3} and n_{N2} are the moles of ammonia molecule and nitrogen molecule (mol), respectively. Then, the mole ratio of atom hydrogen and atom nitrogen is given as:

$$n_H/n_N = 3\phi/(\phi + 7.14) \quad (4)$$

where n_H and n_N are the moles of hydrogen and nitrogen atom (mol), respectively. It can be seen that the relation between the mole ratio of the hydrogen and nitrogen atom and the equivalence ratio shows a nonlinear behavior. Moreover, based on the principle of LIBS, the intensity ratio of two atomic lines is proportional to the concentration ratio of corresponding atoms. As a result, the correlations between the PIRs of H656/N746 and the equivalence ratios of ammonia-nitrogen mixture can be fitted by the following equation:

$$PIR = a\phi(\phi + b) \quad (5)$$

where a and b are constants. The dashed lines in Fig. 5 show the calculated results by Eq. (5). The R^2 of calibration curves at different pressures are all over 0.99, i.e. the PIR of H656/N746 can accurately quantify the equivalence ratio of the ammonia-nitrogen mixture. In addition, the PIRs show a deviation of 3-7% from the mean value, indicating a high measurement precision. The total measurement uncertainties of LIBS

concentration measurements are estimated to be 5-10% by considering the inaccuracy in the equivalence ratio calibrations and the laser pulse instability [32].

3. Results and discussion

3.1. Jet characteristics by Schlieren image

In this section, the Schlieren images of ammonia jets at different injection and ambient conditions are presented. The time dependence of jet characteristics is analyzed in detail, including tip penetration and jet angle which are influential factors on the fuel-air mixing process in DI engines.

Figure 6 shows the Schlieren images of ammonia jets at different time after the start of injection (t_{ASOI}) at the injection pressure of 8.0 bar and the ambient pressure of 2.0 bar. The top and bottom rows are the instantaneous images and corresponding average images for five injections, respectively. As shown in Fig. 6, after the needle starts to lift, the ammonia gas comes out of the nozzle hole and the jet penetrates rapidly. At t_{ASOI} = 0.1 ms, the jet is relatively narrow, probably due to a tiny flow area of ammonia gas at the early stage of the needle lifting process. In the instantaneous images, the asymmetrical jet structures with high fluctuations are clearly observed. The jet edge and jet tip are significantly bent by strong turbulence. A stream of fuel gas is squeezed out of the jet at t_{ASOI} = 2.0 ms. For the gas injection with the PR larger than the critical pressure ratio (1.84 for ammonia), the gas flow is chocked in the nozzle hole, and therefore the complex shock structures are induced near the nozzle exit, making the jet highly turbulent. It was reported that the ambient air would be entrained into the gaps between the large-scale turbulent structures along the jet boundaries and jet tips, effectively promoting the fuel-air mixing during the end of injection (EOI) transients [34].

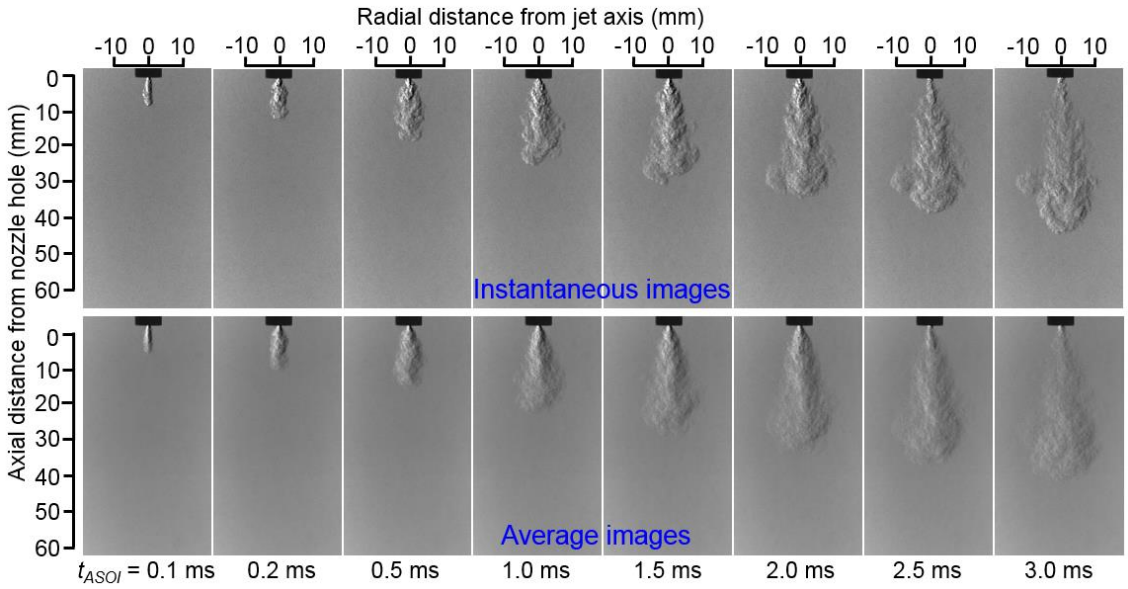

Fig. 6. Instantaneous and averaged Schlieren images of ammonia jets at different t_{ASOI} (P_{inj} = 8.0 bar, P_a = 2.0 bar, T_a = 298 K, τ = 2.0 ms).

The jet tip penetration and jet angle are determined based on the Schlieren images and the image processing procedures. Figure 7 depicts the time evolutions of averaged tip penetration and jet angle of ammonia jets at the injection pressure of 8.0 bar and the ambient pressure of 2.0 bar. The error bars represent the standard deviations for five injections. The time evolution of tip penetration shows an approximately linear trend before t_{ASOI} = 0.1 ms. After that, the tip penetration speed gradually decreases due to the momentum exchange between the high-speed jet and the ambient gas. The time evolution of jet angle shows a transient stage before t_{ASOI} = 0.4 ms, during which the jet angle increases. This is consistent with the narrow jet at t_{ASOI} = 0.1 ms observed in Fig. 6. After t_{ASOI} = 0.4 ms, the jet angle gradually decreases. In addition, relatively larger fluctuations of jet angles can be observed after the EOI due to the weak Schlieren effects around the jet tail. Although the instantaneous images of ammonia jets involve remarkable turbulence as shown in Fig. 6, the error bars of both tip penetration and jet angle in Fig. 7 are quite small, indicating high repeatability of the tests.

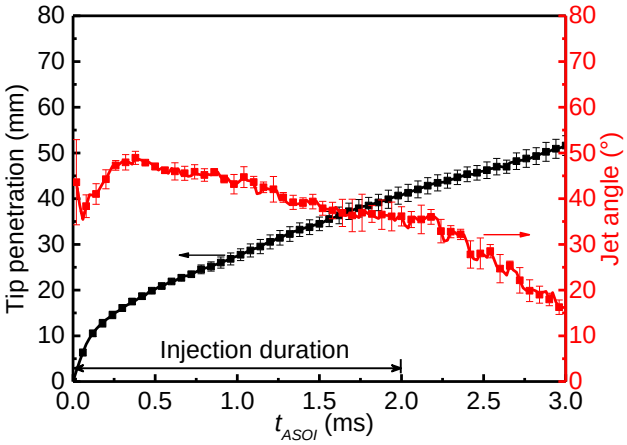

Fig. 7. Time evolutions of averaged tip penetration and jet angle of ammonia jets for five injections (P_{inj} = 8.0 bar, P_a = 2.0 bar, T_a = 298 K, τ = 2.0 ms).

Figure 8 shows the time evolution of tip penetration at different stages. The injection and ambient pressures are 8.0 bar and 2.0 bar, respectively. The logarithmic coordinates are used here to exhibit more clearly the time dependence characteristics of tip penetration. In general, a three-stage behavior of jet tip penetration can be significantly observed. Stage 1 is from the start of injection to about t_{ASOI} = 0.7 ms. During the Stage 1, the tip penetration firstly exhibits a t dependence before approximately t_{ASOI} = 0.1 ms, and then the slope of the curve decreases gradually. The linear behavior of the time evolution of tip penetration at the beginning of injection for gas jets has also been observed by Gerold et al. [35]. Moreover, the tip penetrations of diesel sprays also exhibit a t dependence before the spray break-up time [36] as below:

$$S = \mathrm{K}_{\nu}(2\Delta P / \rho_a)^{0.5} t_{ASOI} \quad (6)$$

where K_{ν} is the model constant, ΔP indicates the pressure difference between the injection pressure and ambient pressure, [Mpa], ρ_f is the fuel density, [kg/m^3], and t_{ASOI} is the time after the start of injection, [ms]. The diesel sprays do not break up completely before the spray break-up time. Consequently, the momentum decay of the spray tip caused by the air resistance is relatively small, leading to a nearly constant-speed penetration during this period. However, the gas jets involve no break-up process. Therefore the fundamental

mechanism of the linear behavior of tip penetration in gas jets at the beginning of injection is different from that in liquid sprays.

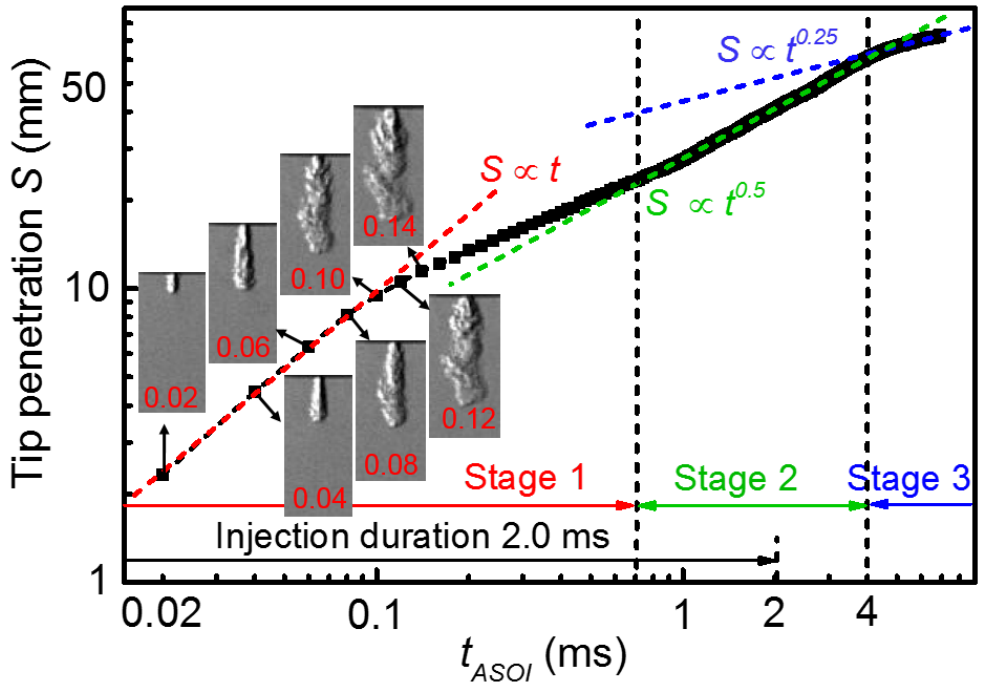

Fig. 8. Three-stage behavior of the tip penetration of ammonia jets. (P_{inj} = 8.0 bar, P_a = 2.0 bar, T_a = 298 K, τ = 2.0 ms).

Some studies showed that the behavior of tip penetration during the initial injection is strongly related to the needle valve movement [37, 38]. At the beginning of the injection, the needle lift is quite small, causing a meager mass flow rate, and the gas flow has not been chocked in the nozzle hole during this period. Therefore the jet involves little shock-induced turbulence. The shock-induced turbulence is also called the Richtmyer–Meshkov instability. It is induced by a shock wave colliding with an interface between two fluids of different density. When two kinds of fluids are impulsively accelerated into each other by the shock wave, small perturbations at the interface gradually evolve into non-linear structures formed of ‘‘bubbles’’ and ‘‘spikes’’. Then, it may lead to the formation of a turbulent mixing zone. The shock-induced turbulence may strongly affect the flow structure and turbulent mixing [39, 40]. As shown in Fig. 8, the jet boundary is smooth before

341 t_{ASOI} = 0.1 ms, but after that it is remarkably disturbed. Lei et al. reported that at the beginning of injection, the
342 turbulence kinetic energy is relatively low both inside and outside the nozzle and then significantly increases
343 after few hundreds of microseconds [41]. As a result of very weak shock-induced turbulence, the ambient air
344 entrainment into the gas jet is dominated by the shear-induced turbulence. Therefore, the momentum exchange
345 between the high-speed jet and ambient air would be small, causing nearly uniform jet tip penetration. This
346 turning point at the end of uniform penetration is named the undisturbed endpoint. After the undisturbed
347 endpoint, the curve slope gradually decreases, indicating that the jet experiences a deceleration process. This
348 is due to the enhanced shock-induced turbulence in gas jets, as shown by the jet images after t_{ASOI} = 0.1 ms in
349 Fig. 8. It should be noted that the behavior of tip penetration at the beginning of injection largely depends on
350 the inner structure of the injector nozzle and therefore can be distinct by using different types of injector. In
351 the studies of Erfan et al. [31] and Dong et al. [42], the tip penetration shows a $t^{0.5}$ dependence at the near
352 nozzle region, but the slope of S-$t^{0.5}$ curve is different from that at the far nozzle region.

353 From about t_{ASOI} = 0.7 ms, the jet goes into the quasi-steady state, which is the main period of jet
354 development. During this stage, the tip penetration correlates well with $t^{0.5}$. Ouellette and Hill [43] developed
355 a model to evaluate the tip penetration of gas jets based on the experimental data and the momentum
356 conservation principle, as shown in Eq. (7):

357 $$S = \Gamma(\dot{M}_n^{\mathrm{g}} / \rho_a)^{0.25} \sqrt{t_{ASOI}} \tag{7}$$

358 $$\dot{M}_n^{\mathrm{g}} = \mathrm{c_d} A_n \rho_n U_n^2 \tag{8}$$

359 where S is the tip penetration [mm], Γ is the penetration constant [-], $\dot{M}_n$ is the momentum injection rate
360 [kg·m/s^2] which can be expressed by Eq. (8). U_n is the choked velocity in nozzle hole [m/s]. A_n is the cross-
361 sectional area of nozzle hole [mm^2]. $\mathrm{c_d}$ is the discharge coefficient [-] and ρ_n is the density of fuel gas at the
362 nozzle hole exit [kg/mm^3]. The momentum injection rate is nearly constant during the quasi-steady state. As a

363 result, the tip penetration has a $t^{0.5}$ dependence. The jet tip decelerates due to significant entrainment of the
364 ambient air produced by both shear-induced turbulence and shock-induced turbulence. Although the gas
365 injection stops at t_{ASOI} = 2.0 ms, the tip penetration behavior after the EOI still keeps consistent with the earlier
366 time until about two times of injection duration. The time dependence of tip penetration during the quasi-
367 steady state at various injection and ambient pressures for different fuel gases will be discussed in detail in the
368 following.

369 It can be observed that another turning point appears at about two times of injection duration. After this
370 turning point, the tip penetration speed decreases more significantly. The behavior of tip penetration exhibits
371 a $t^{0.25}$ dependence until the end of camera recording. The available camera recording time mainly varies with
372 the ambient pressure due to more significant Schlieren effects at the higher ambient pressures (e.g.
373 approximately 7.0 ms at P_a = 2.0 bar). The transitions of tip penetration from a square-root dependence on
374 time to a fourth-root dependence at two times of injection duration have also been observed in diesel sprays
375 by some researchers [44, 45], but rarely reported in gas jets. This phenomenon can be explained by the
376 entrainment wave theory [46]. After the EOI, the deceleration state of diesel jet would travel from the nozzle
377 to the jet tip with increased entrainment rate. After the front of entrainment wave arrives at the jet tip, the
378 whole diesel jet goes into the deceleration state. As a consequence, the jet tip penetration gradually correlates
379 with the fourth-root of time.

380 The effects of injection pressure and ambient pressure on tip penetration and jet angle of ammonia jets
381 are shown in Figs. 9 and 10, respectively. The tip penetrations and jet angles are the averaged values, and the
382 error bars stand for the standard deviations for five tests. As shown in Fig. 9, the time evolutions of tip
383 penetration at different injection pressures keep consistent trends. The tip penetration is increased with the
384 injection pressure increasing. As the injection pressure rises from 5.0 bar to 8.0 bar, the tip penetration at t_{ASOI}

= 3.0 ms increases from 33 mm to 52 mm. This can be attributed to the larger gas density at the higher injection pressure, and therefore the increased momentum flow rate of ammonia gas in the nozzle hole. The jet angle and injection pressure are generally negatively correlated, but this correlation is very weak. At the higher injection pressure, the jets are more likely to develop toward the jet axial direction and contract at the radial direction, causing a lower jet angle. In Fig. 10, it can be seen that the ambient pressure shows more significant effects on the tip penetration and jet angle compared to the injection pressure as shown in Fig. 9. With an increase in the ambient pressure, the tip penetration reduces while the jet angle increases. At t_{ASOI} = 3.0ms, the tip penetration decreases from nearly 76 mm at 1.0 bar to about 24 mm at 4.0 bar. The effects of ambient pressure can be attributed to two aspects. On one hand, the higher ambient pressure will cause the lower pressure ratio, leading to the lower momentum of fuel gas. On the other hand, the ambient pressure also affects ambient density, which has a major role on the entrainment effects. At the higher ambient density, the resistance from ambient gas is increased, therefore, the ammonia jets tend to develop toward the radial direction.

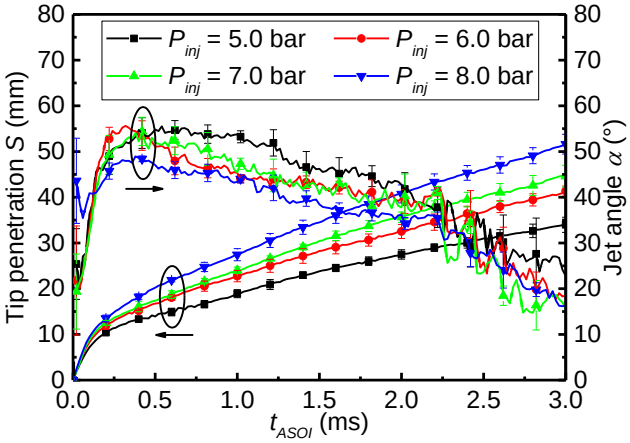

Fig. 9. The effects of injection pressure on tip penetration and jet angle of ammonia jets (P_a = 2.0 bar, T_a = 298 K, τ = 2.0 ms).

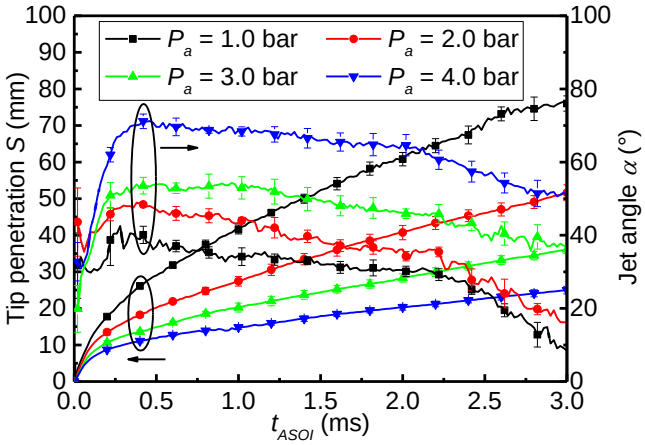

401

402 **Fig. 10.** The effects of ambient pressure on tip penetration and jet angle of ammonia jets (P_{inj} = 8.0 bar, T_a =

403 298 K, τ = 2.0 ms).

404 Figures 11(a) and (b) show the fits of (a) tip penetrations S and (b) $S/(\rho_n/\rho_a)^{0.25}$ with the square root of

405 t_{ASOI} at different PRs. The dots in Fig. 11(a) are the raw data, and the dashed lines are the fitted curves of linear

406 correlations between tip penetration and the square root of t_{ASOI}. Here, the results before t_{ASOI} = 4.0 ms are

407 employed since the time dependence of tip penetration changes after t_{ASOI} = 4.0 ms. Generally, the tip

408 penetrations show linear correlations with the square root of time at different PRs. All coefficients of

409 determination (R^2) are over 0.99. Significant deviations of experimental data with the fitted curves are observed

410 at the early stage of injection, which is consistent with the analysis in Fig. 8. It is found that the duration of

411 this deviation greatly depends on the ambient pressure, probably owing to the effects of ambient pressure on

412 the needle lift-off process. In addition, it can be seen that the slope of the fitted curve increases with the

413 increased PR. At the PR of 2.0, the tip penetrations are quite close despite the different injection and ambient

414 pressures. Ouellette and Hill [43] established an empirical formula for the tip penetration and time scales in

415 underexpanded flow. The jet tip penetration is considered as a function of the gas density at the nozzle exit

416 (ρ_n), ambient gas density (ρ_a) and time after the start of injection (t_{ASOI}) as:

417 $$S/(\rho_n/\rho_a)^{0.25} \propto t_{ASOI}^{0.5} \quad (9)$$

As shown in Fig. 11(b), the results at different PRs generally present similar evolution law. Slight deviations can be observed at the low PRs since the flows are close to the subsonic condition at the PR of 2.0.

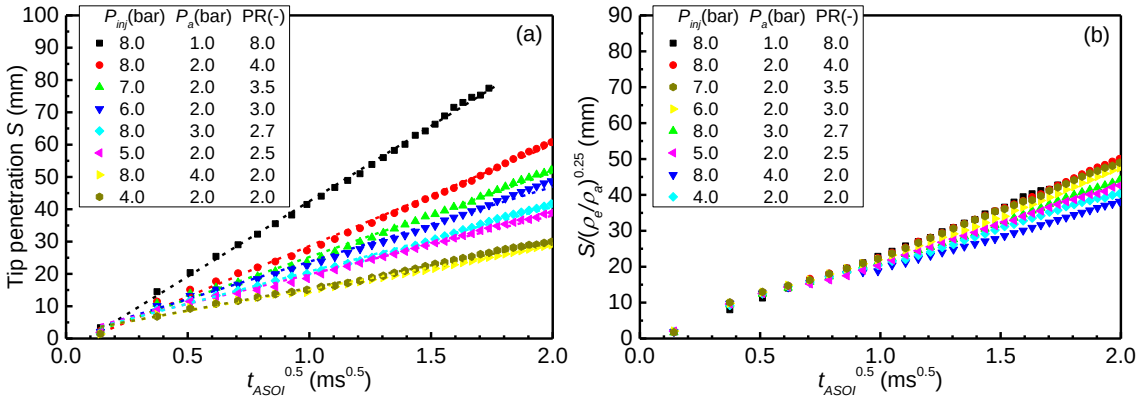

Fig. 11. Fits of (a) tip penetrations S and (b) $S/(\rho_n/\rho_a)^{0.25}$ with the square root of t_{ASOI} at different PRs (T_a = 298 K, τ = 2.0 ms).

3.2. Fuel concentrations of ammonia jets

Figure 12 shows the single-shot and the averaged equivalence ratios and the flammable mixture percentage at different axial positions in ammonia jets. Each black circle indicates an equivalence ratio obtained by a single laser shot. The averaged results of 60 times laser shots are marked by the black solid line. The flammable mixture percentage is defined as the times in which the measured equivalence ratio is within the flammability limit divided by the total measured times (60), and it is indicated by the blue dashed line. The flammability limit for ammonia represented by the red dashed line is considered to be 0.63-1.40 at the pressure of 1.0 bar and temperature of 298 K [2]. It is observed that the averaged equivalence ratio reduces with the increased axial distance from nozzle exit due to the sufficient fuel-air mixing, and the decrease rate of equivalence ratio becomes slow. The single-shot equivalence ratios at each axial position distribute in a wide range, indicating the remarkable fluctuations of fuel concentration in ammonia jets. This is consistent with the previous results in which significant shot-to-shot fluctuations of fuel concentration in natural gas jets were

observed [28, 47]. Generally, the gas jets would involve greater shot-to-shot variations than the liquid sprays due to the instability in the gas expansion process and the inefficient fuel-air mixing [48].

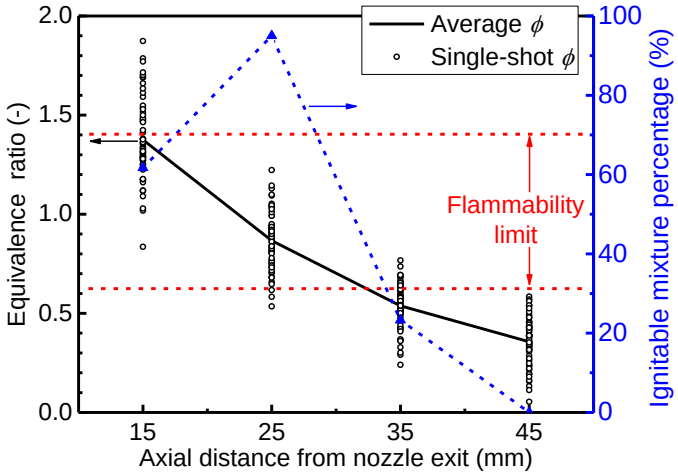

Fig. 12. The single-shot and the averaged equivalence ratios and the ignitable mixture percentage at different axial positions in ammonia jets (P_{inj} = 8.0 bar, P_a = 1.0 bar, t_{ASOI} = 2.0 ms, τ = 2.0 ms).

At 15 mm from the nozzle exit, the single-shot equivalence ratios widely distribute between 0.8 and 1.9 with an average of about 1.4, and 62% of the mixture is flammable. With the axial distance increasing, the flammable mixture percentage firstly increases and then gradually reduces to zero. At 25 mm from nozzle exit, the averaged equivalence ratio is 0.9 and up to 95% of the mixture is flammable, indicating a potentially optimal ignition position within the four measuring positions. When the axial distance increases to 35 mm, the averaged equivalence ratio is below the lower flammability limit, although the mixture is flammable in some laser shots. The mixture becomes totally non-flammable at 45 mm from the nozzle exit.

Figure 13 shows the axial distributions of equivalence ratio in ammonia jets at different injection pressures. The equivalence ratios are the averaged results, and the error bars represent the standard deviations for 60 tests. It is reported that the axial variations of flow variables (e.g., fuel concentration and temperature) in the far-field follow the hyperbolic decay [49, 50]. As a result, the axial distributions of equivalence ratio are fitted by the hyperbolic curves, as shown in Fig. 13 by the dashed lines. The R^2 of the fitted curves at different injection

pressures are larger than 0.98, confirming the hyperbolic decay of fuel concentration along the jet centerline. It can be seen that the equivalence ratios increase with the increased injection pressure at all four measuring positions. In addition, there is no significant difference in fluctuations of equivalence ratio among the three injection pressures. For the under-expanded gas jets, the flow in the injector hole is considered to reach its critical conditions, i.e., the sonic speed and the critical pressure ratio in the throat of injector nozzle. As a result, the mass flow rate of fuel gas in the nozzle hole proportionally increases with the injection pressure. Although the air entrainment is stronger at the higher injection pressure, the mass flow rate increases more quickly, leading to the larger equivalence ratios at the higher injection pressure.

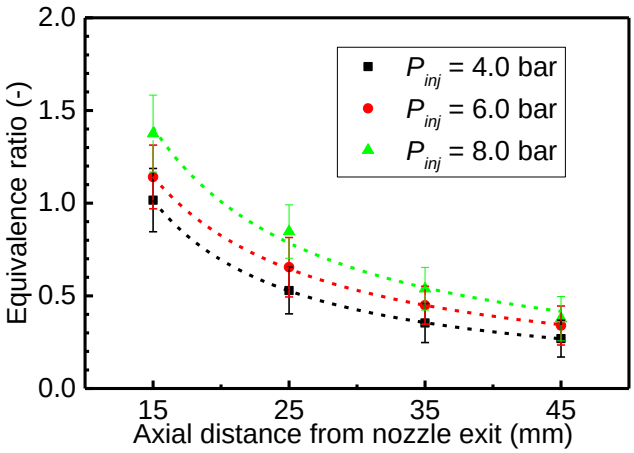

Fig. 13. The axial distributions of equivalence ratio in ammonia jets at different injection pressures (P_a = 1.0 bar, t_{ASOI} = 2.0 ms).

Figure 14 depicts the effects of ambient pressure on the equivalence ratio in ammonia jets. The injection pressure was kept at 8.0 bar, and the measuring position is 25 mm below the nozzle exit. The standard deviations of the equivalence ratio indicated by the error bars are approximately 20% of the mean value at different ambient pressures. Generally, the equivalence ratios gradually reduce with the increased ambient pressure, and the decrease rate becomes slower. At the ambient pressure of 1 bar, the averaged equivalence ratio falls within the flammable limit. The mixture at P_a = 2.0 bar is over-lean, indicating more NO emission

would yield during combustion. When the ambient pressure is higher than 2.0 bar, the mixture turns to be non-flammable. Since the flow is chocked in the injector hole, the mass flow rate of fuel gas is mainly dependent on the upstream pressure. Although the mass flow rate is not entirely independent of the ambient pressure, it does not change considerably at different ambient pressures [31]. Therefore, when the injection pressure is constant, the mass flow rate of fuel gas is considered to be very close at different ambient pressures. Moreover, the air entrainment into the ammonia jet significantly increases at the higher ambient pressure due to both the higher air density and the larger jet angle. Consequently, the fuel concentrations are decreased at the higher ambient pressure.

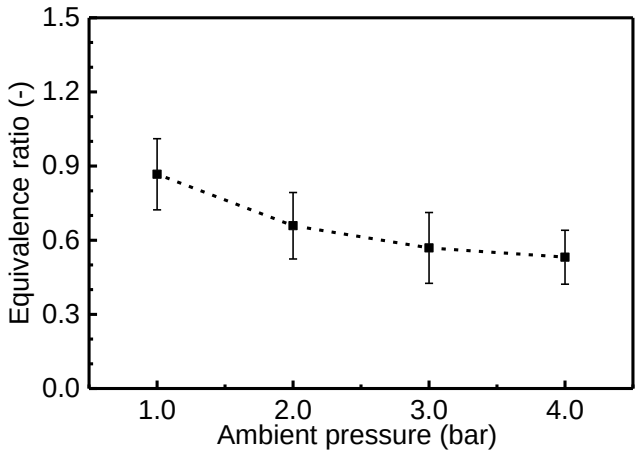

Fig. 14. The effects of ambient pressure on the equivalence ratio in ammonia jets at the injection pressure of 8.0 bar (z = 25 mm, P_{inj} = 8.0 bar, t_{ASOI} = 2.0 ms).

3.3. Comparisons of ammonia and methane jets

Figure 15 shows comparisons of the tip penetration and jet angle between ammonia and methane jets. The error bars in Fig. 15 represent the standard deviations for the average of five tests. The injection pressure was kept at 8.0 bar, and two ambient pressures of 1.0 bar and 4.0 bar (PR = 2.0 and 8.0) were investigated. Generally, Fig. 15 shows that the time evolutions of tip penetration in ammonia jets are pretty similar to those in methane jets at the ambient pressures of both 1.0 bar and 4.0 bar. As shown in Eqs. (6) and (7), the tip

penetration is proportional to the fourth root of the fuel gas density. The gas density is proportional to the gas molar mass at the constant gas pressure and temperature according to the ideal gas equation. Since the molar mass of ammonia (17 g/mol) is very close to that of methane (16 g/mol), their tip penetrations are nearly equivalent. At P_a = 1.0 bar, the tip penetrations, and the jet angles between ammonia and methane jets are nearly equal at different t_{ASOI}. Their jet angles gradually decrease as the jets develop. At the P_a = 4.0 bar, the time evolutions of tip penetrations and the jet angles between ammonia and methane jets are still consistent during the injection. Only slight separation occurs after the EOI, which could be attributed to the slight difference in molar mass between ammonia and methane. Generally, the time evolutions of ammonia and methane jet characteristics, in terms of both tip penetration and jet angle, are quite similar. Consequently, methane could be employed as a substitute for ammonia to study the macroscopic characteristic of ammonia jets, especially for the under-expanded flow with the high PRs. This is critical since ammonia is very corrosive, and thus the ammonia experiments would encounter significant challenges.

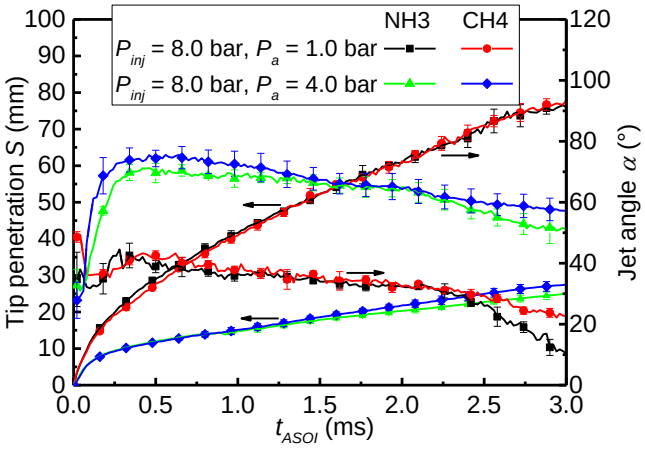

Fig. 15. Comparisons of tip penetration and jet angle between ammonia and methane jets at different ambient pressures (P_{inj} = 8.0 bar, T_a = 298 K, τ = 2.0 ms).

The comparisons of tip penetration as a function of the square root of t_{ASOI} between ammonia and methane jets at different PRs are depicted in Fig. 16. Four PRs from 2.0 to 8.0 were investigated. The black and red

dots represent the results of ammonia and methane, respectively. Tip penetrations of both ammonia and methane jets at different PRs linearly increase with the square root of t_{ASOI} increasing. Despite slight differences at the late stage of jet development, the tip penetrations of ammonia and methane jets are almost equivalent.

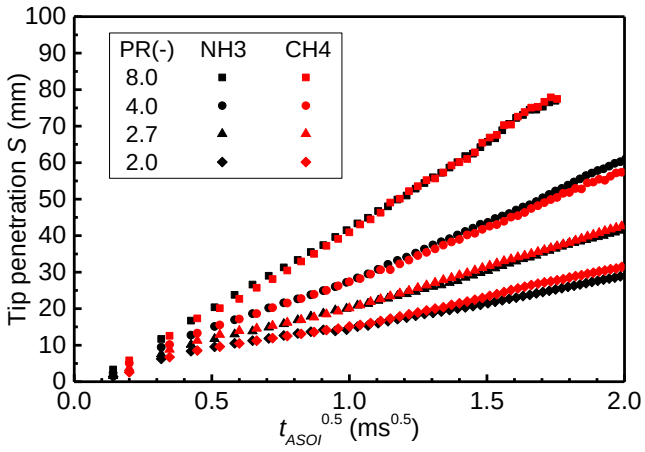

Fig. 16. Comparisons of time evolutions of tip penetration between ammonia and methane jets at different PRs (T_a = 298 K, τ = 2.0 ms).

The comparisons of axial equivalence ratio distributions, and fuel mole fractions between ammonia and methane jets are depicted in Figs. 17 (a) and (b), respectively. The injection and ambient pressures are 8.0 bar and 1.0 bar, respectively. In Fig. 17 (a), the solid dots are the averaged equivalence ratios for 60 tests, and the dashed lines represent the hyperbolic curve fits. It can be seen that the axial distributions of equivalence ratio in both ammonia and methane jets fall well within the hyperbolic decay. Apparently, the equivalence ratios in methane jets are significantly higher than those in ammonia jets. Although the error bars of equivalence ratio in methane jets are wider than those in ammonia jets, the relative standard deviations (standard deviations for the single tests divided by the mean values) are similar for ammonia and methane jets. The flammability limit for methane is considered to be 0.5-1.7 at the pressure of 1.0 bar and temperature of 298 K [2]. For the methane jets, the equivalence ratios at 15 mm and 25 mm below the nozzle exit are beyond the flammability limit. The methane-air mixture is flammable downstream of 30 mm below the nozzle exit. In addition, the equivalence

ratio at 45 mm below the nozzle exit is around 1.1, in favor of a faster flame propagation if the mixture is ignited here. However, the equivalence ratios in ammonia jets are significantly lower than those in methane jets. From the perspective of fuel concentration, the flammable mixture distributions in methane jets are quite different from those in ammonia jets. However, when the equivalence ratios are converted to the mole fractions of fuel gas, the axial distribution of fuel mole fraction in ammonia jets is very close to that in methane jets, as shown in Fig. 17 (b). At the stoichiometric conditions, one mole of ammonia consumes three quarters of a mole of oxygen molecule, while one mole of methane consumes two moles of oxygen molecule. As a consequence, for the same mole fraction of fuel gas, the equivalence ratio of methane-air mixture is 2.7 times that of ammonia-air mixture, leading to the distinct flammable mixture distributions in ammonia and methane jets. These results are very critical for researchers and engineers in calibrating numerical models and determining the proper ignition and diffusion combustion for DI ammonia jets.

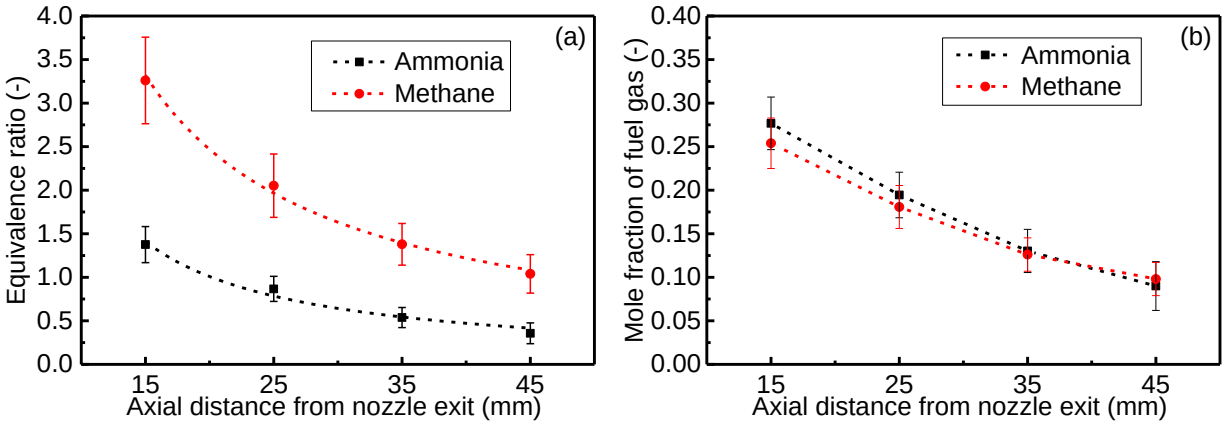

Fig. 17. The comparisons of axial distributions of (a) equivalence ratio and (b) fuel mole fraction between ammonia and methane jets (P_{inj} = 8.0 bar, P_a = 1.0 bar, t_{ASOI} = 2.0 ms).

Fuel-air mixing efficiency in gas jets is mainly controlled by the large-scale turbulent motion induced by the shock and shear force and the small-scale motion for molecular mixing in the jet. In general, the large-scale turbulent motion not only entrains surrounding air into the jet, but also gives turbulent energy for the jet, which is necessary for molecular mixing with small-scale motion in the subsequent mixing process. The Reynolds

number at the nozzle exit in the ammonia jet under the injection pressure of 8.0 bar (≈130000) is close to that in the methane jet (≈120000), showing the similar turbulence intensity. Homogeneous mixture formation is mainly dependent on the molecular mixing in the small-scale motion. The diffusion coefficient between the fuel gas and air is a critical parameter in the molecular mixing process. Since the diffusion coefficient of ammonia in air (0.1978 cm^2/s at 273 K and 1.0 bar) is similar to that of methane in air (0.1952 cm^2/s at 273 K and 1.0 bar), their molecular mixing process is expected to be similar.

4. Conclusions

The macroscopic characteristics of ammonia jets including tip penetration and jet angle have been investigated by using a high-speed Schlieren imaging system. Moreover, the fuel concentrations in ammonia jets have been quantitatively measured by the LIBS technique to study the ammonia-air mixing process. Tests in methane jets have been also conducted for the comparisons. The major conclusions are summarized as follows:

- The time evolution of tip penetration shows a three-stage behavior. The tip penetration exhibits a t, $t^{0.5}$ and $(t-\tau)^{0.25}$ dependence corresponding to the very early stage of injection, the quasi-steady stage and after two times of injection duration, respectively.
- The tip penetration shows a t dependence at the very early injection stage, which might be attributed to the jets involving little shock-induced turbulence and, therefore, having few momentum exchanges with the ambient gas.
- During the quasi-steady state, the jet tip penetration is linearly correlated with the square root of t under different PRs. Besides, the jet tip penetration greatly depends on the pressure ratio.

- In general, the time evolutions of tip penetration and jet angle for ammonia and methane jets are quite similar due to the close molar mass. Consequently, methane can be employed as a substitute of ammonia to study the macroscopic characteristic of ammonia jets.
- The hyperbolic decays of fuel concentrations at the jet axis in both ammonia and methane jets are confirmed experimentally.
- The fuel concentrations in ammonia jets increase with the increased injection pressure due to the larger mass flow rate of fuel gas. However, they significantly reduce with the increased ambient pressure because of the higher air density.
- The axial distributions of fuel mole fraction are nearly equivalent in ammonia and methane jets at the same injection and ambient conditions. However, the equivalence ratios in methane jets are significantly higher than those in ammonia jets, leading to the distinct flammable mixture distributions in ammonia and methane jets.

Acknowledgments

The financial supports by the National Natural Science Foundation of China (51776125) and the Major International (Regional) Joint Research Project of National Natural Science Foundation of China (52020105009) are gratefully acknowledged. The contributions by the graduate students in the Large Engine Research Center of NAOCE in SJTU are highly appreciated.

Reference

[1] Nations U. The Paris Agreement. 2015; available at http://unfccc.int/files/essential_background/convention/application/pdf/english_paris_agreement.pdf.

[2] Kobayashi H, Hayakawa A, Somarathne KDKunkuma A, Okafor Ekenechukwu C. Science and technology of ammonia combustion. Proc Combust Inst 2019;37:109-33.

[3] Aasadnia M, Mehrpooya M. Large-scale liquid hydrogen production methods and approaches: A review. Appl Energy 2018;212:57-83.

[4] Zamfirescu C, Dincer I. Using ammonia as a sustainable fuel. J Power Sources 2008;185:459-65.

[5] Valera-Medina A, Xiao H, Owen-Jones M, David WIF, Bowen PJ. Ammonia for power. Prog Energ Combust 2018;69:63-102.

[6] Kroch E. Ammonia - A fuel for motor buses. J Inst Petrol 2020;31:21-32.

[7] Boothroyd RG. A proposed Australian transition to an anhydrous ammonia fuel transport economy to replace liquid petroleum fuels. WIT Trans Ecol Environ 2014;186:443-56.

[8] Zamfirescu C, Dincer I. Ammonia as a green fuel and hydrogen source for vehicular applications. Fuel Process Technol 2009;90:729-37.

[9] Mørch CS, Bjerre A, Gøttrup MP, Sorenson SC, Schramm J. Ammonia/hydrogen mixtures in an SI-engine: Engine performance and analysis of a proposed fuel system. Fuel 2011;90:854-64.

[10] Hayakawa A, Goto T, Mimoto R, Arakawa Y, Kudo T, Kobayashi H. Laminar burning velocity and Markstein length of ammonia/air premixed flames at various pressures. Fuel 2015;159:98-106.

[11] Mathieu O, Petersen EL. Experimental and modeling study on the high-temperature oxidation of Ammonia and related NOx chemistry. Combust Flame 2015;162:554-70.

[12] Mei B, Zhang X, Ma S, Cui M, Guo H, Cao Z, et al. Experimental and kinetic modeling investigation on the laminar flame propagation of ammonia under oxygen enrichment and elevated pressure conditions. Combust Flame 2019;210:236-46.

599 [13] Westlye FR, Ivarsson A, Schramm J. Experimental investigation of nitrogen based emissions from an
600 ammonia fueled SI-engine. Fuel 2013;111:239-47.
601 [14] Pochet M, Truedsson I, Foucher F, Jeanmart H, Contino F. Ammonia-hydrogen blends in homogeneous-
602 charge compression-ignition engine. SAE paper 2017-24-0087; 2017.
603 [15] Lhuillier C, Brequigny P, Contino F, Mounaïm-Rousselle C. Experimental study on
604 ammonia/hydrogen/air combustion in spark ignition engine conditions. Fuel 2020;269:117448.
605 [16] Frigo S, Gentili R. Analysis of the behaviour of a 4-stroke Si engine fuelled with ammonia and hydrogen.
606 Int J Hydrogen Energ 2013;38:1607-15.
607 [17] Reiter AJ, Kong S-C. Combustion and emissions characteristics of compression-ignition engine using
608 dual ammonia-diesel fuel. Fuel 2011;90:87-97.
609 [18] Tay KL, Yang W, Chou SK, Zhou D, Li J, Yu W, et al. Effects of injection timing and pilot fuel on the
610 combustion of a kerosene-diesel/ammonia dual fuel engine: A numerical study. Energy Procedia
611 2017;105:4621-6.
612 [19] Boretti A. Novel dual fuel diesel-ammonia combustion system in advanced TDI engines. Int J Hydrogen
613 Energ 2017;42:7071-6.
614 [20] Lamas MI, Rodriguez CG. Numerical model to analyze Nox reduction by ammonia injection in diesel-
615 hydrogen engines. Int J Hydrogen Energ 2017;42:26132-41.
616 [21] Reiter AJ, Kong S-C. Demonstration of compression-ignition engine combustion using ammonia in
617 reducing greenhouse gas emissions. Energ Fuel 2008;22:2963-71.
618 [22] Tay KL, Yang W, Li J, Zhou D, Yu W, Zhao F, et al. Numerical investigation on the combustion and
619 emissions of a kerosene-diesel fueled compression ignition engine assisted by ammonia fumigation. Appl
620 Energy 2017;204:1476-88.

621 [23] Grannell SM, Assanis DN, Bohac SV, Gillespie DE. The fuel mix limits and efficiency of a stoichiometric,
622 ammonia, and gasoline dual fueled spark ignition engine. J Eng Gas Turb Power 2008;130:042802.
623 [24] Ryu K, Zacharakis-Jutz GE, Kong S-C. Effects of gaseous ammonia direct injection on performance
624 characteristics of a spark-ignition engine. Appl Energy 2014;116:206-15.
625 [25] Yapicioglu A, Dincer I. Experimental investigation and evaluation of using ammonia and gasoline fuel
626 blends for power generators. Appl Therm Eng 2019;154:1-8.
627 [26] Gross CW, Kong S-C. Performance characteristics of a compression-ignition engine using direct-injection
628 ammonia-DME mixtures. Fuel 2013;103:1069-79.
629 [27] Ryu K, Zacharakis-Jutz GE, Kong S-C. Performance characteristics of compression-ignition engine using
630 high concentration of ammonia mixed with dimethyl ether. Appl Energy 2014;113:488-99.
631 [28] Zhang Z, Li T, Shi W. Ambient tracer-LIF for 2-D quantitative measurement of fuel concentration in gas
632 jets. Energy 2019;171:372-84.
633 [29] Yu J, Vuorinen V, Hillamo H, Sarjovaara T, Kaario O, Larmi M. An experimental investigation on the
634 flow structure and mixture formation of low pressure ratio wall-impinging jets by a natural gas injector. J Nat
635 Gas Sci Eng 2012;9:1-10.
636 [30] Wilkes JA, Danehy PM, Nowak RJ. Fluorescence imaging study of transition in underexpanded free jets.
637 International Congress on Instrumentation in Aerospace Simulation Facilities IEEE 2005:1-8.
638 [31] Erfan I, Chitsaz I, Ziabasharhagh M, Hajialimohammadi A, Fleck B. Injection characteristics of gaseous
639 jet injected by a single-hole nozzle direct injector. Fuel 2015;160:24-34.
640 [32] Zhang Z, Li T, Xue X, Huang S. Simultaneous measurements of fuel concentration and temperature in
641 gas jets by laser induced breakdown spectroscopy. Spectrochim Acta B At Spectrosc 2019;161:105706.

642 [33] Zhang Z, Li T, Huang S. Influence of the pressure and temperature on LIBS for gas concentration
643 measurements. Spectrochim Acta B At Spectrosc 2019;155:24-33.
644 [34] Hu B, Musculus MPB, Oefelein JC. The influence of large-scale structures on entrainment in a
645 decelerating transient turbulent jet revealed by large eddy simulation. Phys Fluids 2012;24:045106.
646 [35] Gerold J, Vogl P, Pfitzner M. New correlation of subsonic, supersonic and cryo gas jets validated by
647 highly accurate schlieren measurements. Exp Fluids 2013;54:1542.
648 [36] Hiroyasu H, Arai M. Structures of fuel sprays in diesel engines. SAE paper 1990-900475; 1990.
649 [37] Chitsaz I, Saidi MH, Mozafari AA, Hajialimohammadi A. Experimental and numerical investigation on
650 the jet characteristics of spark ignition direct injection gaseous injector. Appl Energy 2013;105:8-16.
651 [38] Vera-Tudela W, Kyrtatos P, Schneider B, Boulouchos K, Willmann M. An experimental study on the
652 effects of needle dynamics on the penetration of a high-pressure methane jet. Fuel 2019;253:79-89.
653 [39] Bai J, Wang T, Liu K, Li L, Zhong M, Jiang Y, et al. Large-eddy simulation of the three-dimensional
654 experiment on richtmyer-meshkov instability induced turbulence. International Journal of Astronomy and
655 Astrophysics 2012;02:28-36.
656 [40] Yu J, Vuorinen V, Kaario O, Sarjovaara T, Larmi M. Visualization and analysis of the characteristics of
657 transitional underexpanded jets. Int J Heat Fluid Fl 2013;44:140-54.
658 [41] Lei Y, Liu J, Qiu T, Li Y, Wang Y, Wan B, et al. Gas jet flow characteristic of high-pressure methane
659 pulsed injection of single-hole cylindrical nozzle. Fuel 2019;257:116081.
660 [42] Dong Q, Li Y, Song E, Fan L, Yao C, Sun J. Visualization research on injection characteristics of high-
661 pressure gas jets for natural gas engine. Appl Therm Eng 2018;132:165-73.
662 [43] Ouellette P, Hill PG. Turbulent transient gas injections. J Fluid Eng 2000;122:743-52.

[44] Sangras R, Kwon OC, Faeth GM. Self-preserving properties of unsteady round nonbuoyant turbulent starting jets and puffs in still fluids. J Heat TRANS-T ASME 2002;124:460-9.

[45] Zhou X, Li T, Lai Z, Wei Y. Modeling diesel spray tip and tail penetrations after end-of-injection. Fuel 2019;237:442-56.

[46] Musculus MPB. Entrainment waves in decelerating transient turbulent jets. J Fluid Mech 2009;638:117-40.

[47] Melaika M, Andersson M, Dahlander P. Methane direct injection in an optical SI engine - comparison between different combustion modes. SAE paper 2019-01-0083; 2019.

[48] Sen AK, Zheng J, Huang Z. Dynamics of cycle-to-cycle variations in a natural gas direct-injection spark-ignition engine. Appl Energy 2011;88:2324-34.

[49] Birch AD, Brown DR, Dodson MG, Swaffield F. The structure and concentration decay of high pressure jets of natural gas. Combust Sci Technol 1984;36:249-61.

[50] Yüceil KB, Ötügen MV. Scaling parameters for underexpanded supersonic jets. Phys Fluids 2002;14:4206-15.

Nomenclature

A	the area of upper half of the jet's projection (mm^2)
A_n	the area of nozzle hole (m^2)
ASOI	after the start of injection
c_d	discharge coefficient (-)
CI	compression-ignition
COP21	Conference of Parties 21

CVV	constant volume vessel
d	the nozzle hole diameter (mm)
DME	dimethyl ether
DI	direct injection
E	laser pulse energy (mJ)
EGR	exhaust gas recirculation
EOI	end of injection
ECU	electronic control unit
fps	frames per second
FWHM	full width at half maximum (nm)
FAR	fuel-air ratio (-)
HCCI	homogeneous charge compression ignition
ICCD	intensified charge coupled device
ICE	internal combustion engine
K_v	model constant
LED	light emitting diode
LIB	laser-induced breakdown
LIBS	laser-induced breakdown spectroscopy
$\dot{M}_n$	momentum injection rate (kg·m/s^2)
n_H	the mole of hydrogen atom (mol)
n_N	the mole of nitrogen atom (mol)
n_{NH3}	the mole of ammonia molecule (mol)

706 n_{N2} the mole of nitrogen molecule (mol)

707 P_a ambient pressure (bar)

708 P_{inj} injection pressure (bar)

709 PIR peak intensity ratio (-)

710 PR pressure ratio (-)

711 R^2 coefficients of determination (-)

712 S tip penetration (mm)

713 SBR signal-to-background ratio (-)

714 SCR selective catalytic reduction

715 SNR signal-to-noise ratio (-)

716 SI spark-ignition

717 t_{ASOI} time after the start of injection (ms)

718 t_a ambient temperature (K)

719 U_n the choked velocity in nozzle hole (m/s)

720 α jet angle (°)

721 τ injection duration (ms)

722 ϕ equivalence ratio (-)

723 Γ penetration constant (-)

724 ρ_f fuel density (kg/m^3)

725 ρ_n the density of fuel gas at the nozzle hole exit (kg/m^3)

726 ΔP pressure difference between the injection pressure and ambient pressure (bar)